Title: Cell patterning by secretion-induced plasma membrane flows

Authors: Veneta Gerganova[1,&], Iker Lamas[1,&], David M. Rutkowski[2,&], Aleksandar Vještica[1], Daniela Gallo Castro[1], Vincent Vincenzetti[1], Dimitrios Vavylonis[2,*] and Sophie G Martin[1,*]

Affiliations:

[1]Department of Fundamental Microbiology, University of Lausanne, CH-1015 Switzerland.

[2]Department of Physics, Lehigh University, Bethlehem PA 18015 USA.

*Correspondence to: sophie.martin@unil.ch; vavylonis@lehigh.edu

[&]These authors contributed equally to this work.

Abstract: Cells self-organize using reaction-diffusion and fluid-flow principles. Whether bulk membrane flows contribute to cell patterning has not been established. Here, using mathematical modelling, optogenetics and synthetic probes, we show that polarized exocytosis causes lateral membrane flows away from regions of membrane insertion. Plasma membrane-associated proteins with sufficiently low diffusion and/or detachment rates couple to the flows and deplete from areas of exocytosis. In rod-shaped fission yeast cells, zones of Cdc42 GTPase activity driving polarized exocytosis are limited by GTPase activating proteins (GAPs). We show that membrane flows pattern the GAP Rga4 distribution and coupling of a synthetic GAP to membrane flows is sufficient to establish the rod shape. Thus, membrane flows induced by Cdc42-dependent exocytosis form a negative feedback restricting the zone of Cdc42 activity.

One Sentence Summary: Exocytosis causes bulk membrane flows that drag associated proteins and form a negative feedback restricting the exocytic site.

Main Text: Cells are highly polarized entities that exhibit one (or several) fronts with distinct lipid and protein plasma membrane composition. Reaction-diffusion systems have come a long way in explaining polarity establishment through positive and negative feedback regulations. For instance, in yeast cells, scaffold-mediated positive amplification of Cdc42 GTPase activity underlies the formation of one (or two) cell fronts (*1-4*), with negative feedback promoting oscillations (*5-7*). Physical processes such as cytoskeletal-driven cortical and cytosolic fluid flows, causing advective protein movements, also play important roles in cell polarization (*8*), and can in principle promote polarity establishment (*9*). Membrane flows are predicted to occur and equilibrate membrane tension between spatially segregated zones of exo- and endocytosis, such as in tip-growth of walled pollen tubes (*10, 11*) or in cell migration, as initially proposed in (*12*). However, even though membrane flows have been observed in migrating amoebae, apicomplexans, amoeboid macrophages and neuronal growth cones (*13-16*), their role in cell patterning has not been explored.

We recently described the use of the CRY2-CIB1 optogenetic system in fission yeast (*2*), where blue light activates the cytosolic photosensor domain CRY2PHR (CRY2) to bind its ligand CIBN, linked to the plasma membrane (PM)-interacting domain of the mammalian protein Rit (RitC). These cells grow by tip extension at one or both cell poles, which are sites of endocytosis and exocytosis promoted by local Cdc42 GTPase activity. While in the dark CIBN-RitC is nearly

uniform at the PM and blue light initially caused uniform CRY2 recruitment, within 5 min both proteins cleared from most interphase cell poles (Fig 1A, Movie 1). Similarly, in pre-divisional cells, CRY2 and CIBN cleared from mid-cell, where exocytosis is targeted, but re-appeared at non-growing cell poles (Fig S1A, Movie 2). CRY2 depletion after 5 min correlated with local levels of Cdc42-GTP, marked by CRIB-3GFP (Fig 1A-B), the secretory vesicle associated Rab11-like GTPase Ypt3 (Fig 1B, S1B), exocyst subunits Exo70 and Exo84 (Fig S1C-D), and with fast depletion rates (Fig S1E). Thus, light-induced changes in CRY2-CIBN interactions provoke their clearance from zones of exocytosis.

CRY2 was not depleted from cell poles upon Brefeldin A (BFA) treatment, which completely stops secretion (*17, 18*), with some cell poles even gaining in CRY2 signal (Fig 1C, S1F-G). CRY2 was also not depleted upon secretion inactivation in the *ypt3-i5* mutant (Fig 1D, S1H). We note that both conditions also caused reduction in CRIB-GFP, perhaps due to loss of positive feedback between growth and polarity (*19*). GFP-Ypt3 intensity was also slightly reduced in BFA-treated cells (Fig S1G). Nevertheless, comparison of cell poles with similar GFP intensity clearly showed that CRY2 does not deplete upon secretion block. Cell poles are also sites of endocytosis, which is strictly dependent on actin patch assembly by the Arp2/3 complex. To test the role of endocytosis, we disrupted all actin structures with Latrunculin A (LatA) in cells lacking the MAPK Sty1, since LatA treatment of WT cells causes MAPK stress signalling and loss of cell polarity (*20*). In LatA-treated *sty1*Δ cells, actin patches were lost, but CRY2 still depleted from cell poles (Fig 1E, S1I). We conclude that CRY2-CIBN depletion can occur by exocytosis alone, but not by endocytosis.

We performed computer simulations to test the hypothesis that deposition and retrieval of membrane material through exo- and endocytic events generates flows strong enough to deplete membrane-associated proteins at growth sites. We modelled proteins as particles with association/dissociation rate constants k_{on} and k_{off}, diffusing on a sphere approximating the cell tip, and displaced by exo/endocytotic events over zones of width σ_{exo} and σ_{endo} (Fig 2A, Movie 3; see Methods section for details). Particles are displaced radially around the site of vesicle delivery/internalization (Fig 2B), as should occur for proteins in fluid membrane components, flowing to accommodate the change of membrane area on a background of membrane tension. To calibrate the model, we measured rates of fission yeast endocytosis (Table S1).

Considering conditions where overall membrane delivery by exocytosis balances internalization by endocytosis, and assuming that neither exocytic nor endocytic vesicles carry membrane-associated proteins, we found tip depletion when exocytosis is narrower than exocytosis, $\sigma_{exo} < \sigma_{endo}$ (Fig 2C, Fig S2A). This is a condition which we verified in cells (Fig S3 and Methods). The active diffusion generated by the randomness of endo- and exocytic events was not by itself sufficient to drive significant concentration gradients when $\sigma_{exo} = \sigma_{endo}$ (Fig S2A, S2C). Under net growth conditions, where exocytosis exceeds endocytosis by the amount of extra membrane needed for cell growth, depletion was stronger and faster, and occurred even when $\sigma_{exo} = \sigma_{endo}$ (Fig S2A-C). Net growth conditions in absence of endocytosis (mimicking growth upon LatA treatment) also led to depletion (Fig S2E). Thus, a membrane flow-based model can reproduce the observed depletion from cell poles.

Using the measured endocytosis and exocytosis profiles in our model, we plotted the tip occupation ratio, a measure of depletion, as a function of k_{off} and diffusion coefficient D (Fig 2D). The model makes two key, testable predictions: First, significant tip depletion requires both

parameters to be sufficiently small – this is the limit where particle movement and exchange are too slow to counteract flow away from the tip (Movies 3, 4). Second, membrane material flowing away from the cell tip accumulates in a region of enhanced density near the end of the depletion area (Fig 2E). Lateral peak formation requires slow diffusion rates (Fig S2D). Both tip depletion and lateral build-up were stronger in conditions of net growth (Fig S2B).

The finding that depletion is only observed for proteins with slow dynamics (low k_{off} or *D*) provides an explanation for the acute change in CIBN localization upon light-induced CRY2 interaction. Indeed, light activation promotes not only CIBN-CRY2 binding but also formation of CRY2 oligomers through a distinct binding interface (*21, 22*). CRY2 oligomers form bright foci (see Fig 1A), predicted to reduce dynamics through clustering of membrane anchors. Using FRAP to estimate *D* and k_{off} (Fig S4), we found that CRY2 interaction causes a >10-fold decrease in CIBN-RitC *D* and k_{off}, to values consistent with tip depletion in the simulations (Fig 3A). CRY2-CIBN tip depletion was more marked in experiments than predicted by the measured *D* and k_{off} values, which we reasoned is due to CRY2 oligomerization not only decreasing membrane-unbinding dynamics but also biasing CRY2 binding from the cytosol. This can be accounted for in the model by increasing the rate of particle dimerization on the membrane, which leads to exacerbated tip depletion (Fig S5). We propose that tip depletion events revealed by optogenetics are due to acute clustering-mediated changes in membrane-binding properties.

Simulations of protein removal by endocytic vesicles neglecting membrane flows, which were previously shown to maintain the polarization of slow-diffusing transmembrane proteins delivered by secretory vesicles (*23*), generate tip depletion for similar, low values of k_{off} and *D*. However, in contrast to membrane flow simulations, they do not produce a lateral accumulation peak (Fig S2F-G). Thus, protein accumulation on the edges of the depletion zone is a characteristic feature of the tip depletion model. Concordant with the flow model, a lateral CRY2 peak corresponding to the edge of the CRIB-labelled depletion zone increased over time (Fig 3B, Fig 1A white arrowhead). The rates of CRY2 levels decrease from cell pole and increase at edges were indistinguishable, suggesting they reflect the same molecular process. Kymographs of CRY2 oligomers at cell tips also directly showed events of flow away from the cell pole (Fig 3C). These observations support the existence of bulk membrane flows carrying associated proteins away from sites of polarized secretion.

To test the role of membrane binding in flow-mediated protein patterning without the amplifying effect of oligomerization, we constructed a series of one, two or three tandem copies of the membrane anchor RitC tagged with sfGFP. Estimated k_{off} and *D* rates extracted from FRAP experiments were higher for 1xRitC than 2xRitC and 3xRitC (Fig 3D). A control 3xsfGFP-1xRitC construct showed only slightly reduced k_{off} compared to sfGFP-1xRitC, suggesting a small effect of protein size or perhaps weak sfGFP-mediated oligomerization. The measured dynamic parameters of 2xRitC and 3xRitC, but not 1xRitC and 3xsfGFP-1xRitC, fall within the range predicted in the model to cause local depletion (Fig 3D). Indeed, cell pole depletion was observed for 2xRitC and more prominently 3xRitC, but not 1xRitC constructs. This is particularly visible in comparison with the uniform localization mCherry-1xRitC co-expressed in these cells (Fig 3E, Movie 5). Signal depletion at cell poles correlated with Cdc42-GTP levels (Fig S6). Thus, membrane affinity is a strong predictor of protein distribution around sites of polarized exocytosis (Fig 3F). The dependence of protein distribution on membrane affinity

should invite careful consideration of this parameter when designing probes to evaluate lipid distribution.

To probe the role of membrane flows in cell patterning, we focused on the Cdc42 GTPase activating protein (GAP) Rga4, which is excluded from cell poles and forms membrane-associated clusters distributed in a 'corset' pattern, reminiscent of the lateral peaks described above (Fig 4A) (*24, 25*). Previous work suggested that cell side-localized Cdc42 GAPs control cell width by restricting the size of the Cdc42 active zone (*24, 26, 27*). Extensive structure-function analysis of GFP-tagged Rga4 fragments, described in Fig S7 and supplemental text, indicated oligomerization by coiled-coils (cc) and the presence of a cortex-binding domain (CBD) comprising two membrane-binding motifs. A minimal cc-CBD Rga4 fragment recapitulated the main features of Rga4 localization, forming clusters partly depleted from cell poles (Fig 4B) and was used to probe how a simplified endogenous protein may be affected by membrane flows. Truncating the coiled coils led to faster membrane-binding dynamics and re-population of the cell poles (CBD only, Fig 4B-D). Tandem multimerization of the CBD (4xCBD) increased membrane affinity and restored depletion from cell poles (Fig 4B-D), as did artificial CBD oligomerization by fusion with CRY2 (Fig S8A). Truncating one of the membrane-binding motifs (cc-CBD-Δ2) to reduce membrane affinity led to faster protein dynamics, as confirmed by FRAP analysis (Fig 4D) and TIRF microscopy (Fig S8B-C, Movie 6-7). This truncation caused enrichment at cell poles (Fig 4B-D), indicating affinity of the coiled coil region for cell poles. Increasing membrane-affinity by multimerization (4x cc-CBD-Δ2) restored tip depletion and enrichment to cell sides (Fig 4B-D). Thus, even with a preferential association at cell poles, the oligomerization and two membrane-binding motifs of Rga4 ensure a sufficiently long membrane residence time that couples Rga4 to membrane flows towards cell sides.

To directly test the importance of the GAP lateral localization, we constructed a synthetic GAP (optoGAP) consisting of CRY2, the membrane-binding RitC, and the Rga4 GAP domain. OptoGAP is predicted to decorate the plasma membrane uniformly in the dark, but couple to membrane flows and deplete from cell poles in the light, due to CRY2 oligomerization. When expressed in the light in cells lacking all endogenous Cdc42 GAPs, which exhibit poor growth and a round morphology with very large zones of Cdc42 activity (*28*), not only was optoGAP depleted from zones of Cdc42 activity (Fig 4E), but the zone size was strongly reduced (Fig 4E, 4H), restoring viability and the rod cell shape (Fig 4I-J). Upon growth in the dark, optoGAP was present around the cell periphery (Fig 4E) and was toxic to the cells (Fig 4J), the majority of which showed no cortical CRIB (Fig 4G) and regained a round morphology (Fig 4I). Further return of these cells to the light led to acute local optoGAP depletion coinciding with a zone of Cdc42 activity, with lateral flow movements captured in kymographs, and outgrowth of a tube of restricted width (Fig 4F, Movie 8). We conclude that coupling of Cdc42 inhibition to membrane flows, which are themselves induced by Cdc42 activity, forms a spatial negative feedback sufficient to restrict zones of Cdc42 activity and define cell width (Fig 4K).

Because membrane flows are a consequence of polarized secretion, they are likely to be prevalent in cells and pattern membrane-associated proteins, coordinating with the cytoskeleton that can independently tune membrane rheology (*29, 30*). Besides Rga4, membrane flows may promote the lateral localization of several proteins that organize the yeast cell shape and division, and explain their exclusion from both cell poles in wildtype cells, but from the only growing pole in monopolar mutants (for instance Rga6, Mid1, Blt1, Cdr2, Skb1 (*25, 27, 31-35*)). Membrane

flows may also help couple endocytosis around sites of exocytosis, which also promote polarity establishment (*36, 37*). Other proteins localize to secretion sites despite membrane flows, thanks to fast membrane unbinding, directed cytoskeletal transport or preferred affinity to static mobile components. For instance, pole-enriched Pom1 shows association to microtubule-transported factors and very fast membrane unbinding dynamics (*38, 39*). The Cdc42 GTPase also has to resist dilution from secretion-derived membrane addition (*40*). These principles of membrane-associated protein patterning are likely valid in all eukaryotic cells. Indeed, precise spatial distribution of exo- and endocytosis, predicted to induce membrane flows, accompanies cellular processes ranging from tip-growth in fungi and pollen tubes (*41*), formation of neuronal connections, cilia and immunological synapses (*42, 43*), cell migration to cytokinesis (*44, 45*). Furthermore, because protein localization can be altered by a simple change in membrane unbinding rates, it may be acutely modified through post-translational modifications that modulate membrane affinity and/or oligomerization.

References and Notes:

1. L. Kozubowski *et al.*, Symmetry-breaking polarization driven by a Cdc42p GEF-PAK complex. *Curr Biol* **18**, 1719-1726 (2008).
2. I. Lamas, L. Merlini, A. Vjestica, V. Vincenzetti, S. G. Martin, Optogenetics reveals Cdc42 local activation by scaffold-mediated positive feedback and Ras GTPase. *PLoS Biol* **18**, e3000600 (2020).
3. A. C. Butty *et al.*, A positive feedback loop stabilizes the guanine-nucleotide exchange factor Cdc24 at sites of polarization. *Embo J* **21**, 1565-1576 (2002).
4. P. Rapali *et al.*, Scaffold-mediated gating of Cdc42 signalling flux. *eLife* **6**, (2017).
5. M. Das *et al.*, Oscillatory Dynamics of Cdc42 GTPase in the Control of Polarized Growth. *Science*, (2012).
6. A. S. Howell *et al.*, Negative feedback enhances robustness in the yeast polarity establishment circuit. *Cell* **149**, 322-333 (2012).
7. C. C. Kuo *et al.*, Inhibitory GEF phosphorylation provides negative feedback in the yeast polarity circuit. *Curr Biol* **24**, 753-759 (2014).
8. R. Illukkumbura, T. Bland, N. W. Goehring, Patterning and polarization of cells by intracellular flows. *Curr Opin Cell Biol* **62**, 123-134 (2020).
9. M. C. Wigbers, F. Brauns, C. Y. Leung, E. Frey, Flow Induced Symmetry Breaking in a Conceptual Polarity Model. *Cells* **9**, (2020).
10. B. Kost, Spatial control of Rho (Rac-Rop) signaling in tip-growing plant cells. *Trends Cell Biol* **18**, 119-127 (2008).
11. G. Grebnev, M. Ntefidou, B. Kost, Secretion and Endocytosis in Pollen Tubes: Models of Tip Growth in the Spot Light. *Frontiers in plant science* **8**, 154 (2017).
12. M. S. Bretscher, Endocytosis: relation to capping and cell locomotion. *Science* **224**, 681-686 (1984).
13. M. Tanaka *et al.*, Turnover and flow of the cell membrane for cell migration. *Scientific reports* **7**, 12970 (2017).
14. P. R. O'Neill *et al.*, Membrane Flow Drives an Adhesion-Independent Amoeboid Cell Migration Mode. *Dev Cell* **46**, 9-22 e24 (2018).
15. S. Gras *et al.*, An endocytic-secretory cycle participates in Toxoplasma gondii in motility. *PLoS Biol* **17**, e3000060 (2019).
16. J. Dai, M. P. Sheetz, Axon membrane flows from the growth cone to the cell body. *Cell* **83**, 693-701 (1995).
17. T. G. Turi, P. Webster, J. K. Rose, Brefeldin A sensitivity and resistance in Schizosaccharomyces pombe. Isolation of multiple genes conferring resistance. *J Biol Chem* **269**, 24229-24236 (1994).
18. M. Marek, V. Vincenzetti, S. G. Martin, Sterol biosensor reveals LAM-family Ltc1-dependent sterol flow to endosomes upon Arp2/3 inhibition. *J Cell Biol* **219**, (2020).
19. D. Bonazzi *et al.*, Symmetry Breaking in Spore Germination Relies on an Interplay between Polar Cap Stability and Spore Wall Mechanics. *Dev Cell* **28**, 534-546 (2014).
20. D. R. Mutavchiev, M. Leda, K. E. Sawin, Remodeling of the Fission Yeast Cdc42 Cell-Polarity Module via the Sty1 p38 Stress-Activated Protein Kinase Pathway. *Curr Biol* **26**, 2921-2928 (2016).

21. L. Duan *et al.*, Understanding CRY2 interactions for optical control of intracellular signaling. *Nat Commun* **8**, 547 (2017).
22. L. J. Bugaj, A. T. Choksi, C. K. Mesuda, R. S. Kane, D. V. Schaffer, Optogenetic protein clustering and signaling activation in mammalian cells. *Nat Methods* **10**, 249-252 (2013).
23. J. Valdez-Taubas, H. R. Pelham, Slow diffusion of proteins in the yeast plasma membrane allows polarity to be maintained by endocytic cycling. *Curr Biol* **13**, 1636-1640 (2003).
24. M. Das *et al.*, Regulation of cell diameter, For3p localization, and cell symmetry by fission yeast Rho-GAP Rga4p. *Mol Biol Cell* **18**, 2090-2101 (2007).
25. H. Tatebe, K. Nakano, R. Maximo, K. Shiozaki, Pom1 DYRK regulates localization of the Rga4 GAP to ensure bipolar activation of Cdc42 in fission yeast. *Curr Biol* **18**, 322-330 (2008).
26. F. D. Kelly, P. Nurse, Spatial control of Cdc42 activation determines cell width in fission yeast. *Mol Biol Cell* **22**, 3801-3811 (2011).
27. M. T. Revilla-Guarinos *et al.*, Rga6 is a Fission Yeast Rho GAP Involved in Cdc42 Regulation of Polarized Growth. *Mol Biol Cell*, (2016).
28. D. Gallo Castro, S. G. Martin, Differential GAP requirement for Cdc42-GTP polarization during proliferation and sexual reproduction. *J Cell Biol* **217**, 4215-4229 (2018).
29. A. Kusumi *et al.*, Dynamic organizing principles of the plasma membrane that regulate signal transduction: commemorating the fortieth anniversary of Singer and Nicolson's fluid-mosaic model. *Annu Rev Cell Dev Biol* **28**, 215-250 (2012).
30. Z. Shi, Z. T. Graber, T. Baumgart, H. A. Stone, A. E. Cohen, Cell Membranes Resist Flow. *Cell* **175**, 1769-1779 e1713 (2018).
31. N. N. Padte, S. G. Martin, M. Howard, F. Chang, The cell-end factor pom1p inhibits mid1p in specification of the cell division plane in fission yeast. *Curr Biol* **16**, 2480-2487 (2006).
32. S. G. Martin, M. Berthelot-Grosjean, Polar gradients of the DYRK-family kinase Pom1 couple cell length with the cell cycle. *Nature* **459**, 852-856 (2009).
33. J. B. Moseley, A. Mayeux, A. Paoletti, P. Nurse, A spatial gradient coordinates cell size and mitotic entry in fission yeast. *Nature* **459**, 857-860 (2009).
34. L. Deng, J. B. Moseley, Compartmentalized nodes control mitotic entry signaling in fission yeast. *Mol Biol Cell* **24**, 1872-1881 (2013).
35. M. Guzman-Vendrell *et al.*, Blt1 and Mid1 provide overlapping membrane anchors to position the division plane in fission yeast. *Mol Cell Biol* **33**, 418-428 (2013).
36. R. T. A. Pedersen, J. E. Hassinger, P. Marchando, D. G. Drubin, Spatial regulation of clathrin-mediated endocytosis through position-dependent site maturation. *J Cell Biol* **219**, (2020).
37. M. Jose, S. Tollis, D. Nair, J. B. Sibarita, D. McCusker, Robust polarity establishment occurs via an endocytosis-based cortical corralling mechanism. *J Cell Biol* **200**, 407-418 (2013).
38. V. Gerganova *et al.*, Multi-phosphorylation reaction and clustering tune Pom1 gradient mid-cell levels according to cell size. *eLife* **8**, (2019).
39. O. Hachet *et al.*, A phosphorylation cycle shapes gradients of the DYRK family kinase Pom1 at the plasma membrane. *Cell* **145**, 1116-1128 (2011).
40. A. T. Layton *et al.*, Modeling vesicle traffic reveals unexpected consequences for Cdc42p-mediated polarity establishment. *Curr Biol* **21**, 184-194 (2011).
41. G. Steinberg, M. A. Penalva, M. Riquelme, H. A. Wosten, S. D. Harris, Cell Biology of Hyphal Growth. *Microbiol Spectr* **5**, (2017).
42. G. M. Griffiths, A. Tsun, J. C. Stinchcombe, The immunological synapse: a focal point for endocytosis and exocytosis. *J Cell Biol* **189**, 399-406 (2010).
43. J. Roos, R. B. Kelly, The endocytic machinery in nerve terminals surrounds sites of exocytosis. *Curr Biol* **9**, 1411-1414 (1999).
44. J. A. Castillo-Badillo, A. C. Bandi, S. Harlalka, N. Gautam, SRRF-Stream Imaging of Optogenetically Controlled Furrow Formation Shows Localized and Coordinated Endocytosis and Exocytosis Mediating Membrane Remodeling. *ACS Synth Biol* **9**, 902-919 (2020).
45. K. S. Gerien, J. Q. Wu, Molecular mechanisms of contractile-ring constriction and membrane trafficking in cytokinesis. *Biophys Rev* **10**, 1649-1666 (2018).
46. H. Brzeska, J. Guag, K. Remmert, S. Chacko, E. D. Korn, An experimentally based computer search identifies unstructured membrane-binding sites in proteins: application to class I myosins, PAKS, and CARMIL. *J Biol Chem* **285**, 5738-5747 (2010).

47. D. T. Gillespie, Exact stochastic simulation of coupled chemical reactions. *J. Phys. Chem.* **81**, 2340–2361 (1977).
48. P. Castro-Villarreal, A. Villada-Balbuena, J. M. Mendez-Alcaraz, R. Castaneda-Priego, S. Estrada-Jimenez, A Brownian dynamics algorithm for colloids in curved manifolds. *J Chem Phys* **140**, 214115 (2014).
49. A. W. McClure *et al.*, Role of Polarized G Protein Signaling in Tracking Pheromone Gradients. *Dev Cell* **35**, 471-482 (2015).
50. H. Cheng *et al.*, Role of the Rab GTP-binding protein Ypt3 in the fission yeast exocytic pathway and its connection to calcineurin function. *Mol Biol Cell* **13**, 2963-2976 (2002).
51. N. Wang, I. J. Lee, G. Rask, J. Q. Wu, Roles of the TRAPP-II Complex and the Exocyst in Membrane Deposition during Fission Yeast Cytokinesis. *PLoS Biol* **14**, e1002437 (2016).
52. J. H. Lee, J. E. Heuser, R. Roth, U. Goodenough, Eisosome Ultrastructure and Evolution in Fungi, Microalgae, and Lichens. *Eukaryot Cell* **14**, 1017-1042 (2015).
53. W. Kukulski, M. Schorb, M. Kaksonen, J. A. Briggs, Plasma membrane reshaping during endocytosis is revealed by time-resolved electron tomography. *Cell* **150**, 508-520 (2012).
54. L. V. Chernomordik, M. M. Kozlov, Mechanics of membrane fusion. *Nature structural & molecular biology* **15**, 675-683 (2008).
55. W. Shin *et al.*, Vesicle Shrinking and Enlargement Play Opposing Roles in the Release of Exocytotic Contents. *Cell reports* **30**, 421-431 e427 (2020).
56. M. Chabanon, J. C. S. Ho, B. Liedberg, A. N. Parikh, P. Rangamani, Pulsatile Lipid Vesicles under Osmotic Stress. *Biophys J* **112**, 1682-1691 (2017).
57. A. E. Cohen, Z. Shi, Do Cell Membranes Flow Like Honey or Jiggle Like Jello? *Bioessays* **42**, (2020).
58. K. D. Moran, D. J. Lew, How Diffusion Impacts Cortical Protein Distribution in Yeasts. *Cells* **9**, (2020).
59. Z. Kalay, T. K. Fujiwara, A. Otaka, A. Kusumi, Lateral diffusion in a discrete fluid membrane with immobile particles. *Phys Rev E* **89**, (2014).
60. B. Fogelson, A. Mogilner, Computational Estimates of Membrane Flow and Tension Gradient in Motile Cells. *Plos One* **9**, (2014).
61. S. S. Andrews, D. Bray, Stochastic simulation of chemical reactions with spatial resolution and single molecule detail. *Phys Biol* **1**, 137-151 (2004).
62. O. N. Yogurtcu, M. E. Johnson, Theory of bi-molecular association dynamics in 2D for accurate model and experimental parameterization of binding rates. *Journal of Chemical Physics* **143**, (2015).
63. B. O'Shaughnessy, D. Vavylonis, Kinetic regimes and cross-over times in many-particle reacting systems. *Europhys Lett* **45**, 653-658 (1999).
64. H. Wang *et al.*, The multiprotein exocyst complex is essential for cell separation in Schizosaccharomyces pombe. *Mol Biol Cell* **13**, 515-529 (2002).
65. J. Ries, C. Klose, C. Walch-Solimena, P. Schwille, How to measure slow diffusion in yeast cell membranes. *Proc Spie* **6991**, (2008).
66. B. P. Ziemba, J. D. Knight, J. J. Falke, Assembly of Membrane-Bound Protein Complexes: Detection and Analysis by Single Molecule Diffusion. *Biochemistry* **51**, 1638-1647 (2012).
67. J. D. Knight, M. G. Lerner, J. G. Marcano-Velazquez, R. W. Pastor, J. J. Falke, Single Molecule Diffusion of Membrane-Bound Proteins: Window into Lipid Contacts and Bilayer Dynamics. *Biophysical Journal* **99**, 2879-2887 (2010).
68. B. A. Camley, F. L. H. Brown, Motion of objects embedded in lipid bilayer membranes: Advection and effective viscosity. *Journal of Chemical Physics* **151**, (2019).
69. J. R. Houser *et al.*, The impact of physiological crowding on the diffusivity of membrane bound proteins. *Soft Matter* **12**, 2127-2134 (2016).
70. D. F. Kucik, E. L. Elson, M. P. Sheetz, Weak dependence of mobility of membrane protein aggregates on aggregate size supports a viscous model of retardation of diffusion (vol 76, pg 314, 1999). *Biophysical Journal* **76**, 1720-1720 (1999).
71. J. Bähler *et al.*, Heterologous modules for efficient and versatile PCR-based gene targeting in Schizosaccharomyces pombe. *Yeast* **14**, 943-951 (1998).
72. A. Vjestica *et al.*, A toolbox of Stable Integration Vectors (SIV) in the fission yeast Schizosaccharomyces pombe. *J Cell Sci*, (2019).
73. F. O. Bendezu, S. G. Martin, Actin cables and the exocyst form two independent morphogenesis pathways in the fission yeast. *Mol Biol Cell* **22**, 44-53 (2011).
74. O. Dudin *et al.*, A formin-nucleated actin aster concentrates cell wall hydrolases for cell fusion in fission yeast. *J Cell Biol* **208**, 897-911 (2015).

75. J. Chow, Correlation Matrix Scatterplot (https://www.mathworks.com/matlabcentral/fileexchange/53043-correlation-matrix-scatterplot). *MATLAB Central File Exchange*, (2020).
76. F. O. Bendezu, V. Vincenzetti, S. G. Martin, Fission yeast Sec3 and Exo70 are transported on actin cables and localize the exocyst complex to cell poles. *PLoS One* **7**, e40248 (2012).
77. J. Q. Wu, J. Bahler, J. R. Pringle, Roles of a fimbrin and an alpha-actinin-like protein in fission yeast cell polarization and cytokinesis. *Mol Biol Cell* **12**, 1061-1077 (2001).
78. V. Sirotkin, J. Berro, K. Macmillan, L. Zhao, T. D. Pollard, Quantitative analysis of the mechanism of endocytic actin patch assembly and disassembly in fission yeast. *Mol Biol Cell* **21**, 2894-2904 (2010).
79. M. Kohli, V. Galati, K. Boudier, R. W. Roberson, P. Philippsen, Growth-speed-correlated localization of exocyst and polarisome components in growth zones of Ashbya gossypii hyphal tips. *J Cell Sci* **121**, 3878-3889 (2008).
80. N. Taheri-Talesh *et al.*, The tip growth apparatus of Aspergillus nidulans. *Mol Biol Cell* **19**, 1439-1449 (2008).
81. D. L. Delgado-Alvarez *et al.*, Visualization of F-actin localization and dynamics with live cell markers in Neurospora crassa. *Fungal Genet Biol* **47**, 573-586 (2010).
82. D. McCusker, A. Royou, C. Velours, D. Kellogg, Cdk1-dependent control of membrane-trafficking dynamics. *Mol Biol Cell* **23**, 3336-3347 (2012).
83. J. Y. Tinevez *et al.*, TrackMate: An open and extensible platform for single-particle tracking. *Methods* **115**, 80-90 (2017).

Acknowledgments: We thank Stephan Gruber (Unil), Jan-Willem Veening (Unil), Serge Pelet (Unil), Laura Merlini (Unil), and Olivia Muriel-Lopez (Unil) for careful reading of the manuscript. **Funding:** This work was funded by an ERC consolidator grant (CellFusion) and a Swiss National Science Foundation grant (310030B_176396) to SGM, and National Institutes of Health Grants R01GM114201 and R35GM136372 to DV. **Author contributions:** IL, VG, AV and SGM conceived the project. IL performed all experiments in Fig 1, 3B-C, S1 and S3. VG performed all other experiments in Fig 3, 4 and S6-8. DMR and DV conceptualized the simulations and FRAP analysis methods. DMR performed all simulations and FRAP analyses. AV performed the initial RitC multimerization experiments. DG performed initial Rga4 structure-function analysis. VV provided technical support. SGM and DV coordinated the project and acquired funding. SGM and DV wrote the first draft of the manuscript, which was revised by all authors. **Competing interests:** Authors declare no competing interests. **Data and materials availability:** All data and reagents are available upon reasonable request to the corresponding authors.

Figure 1

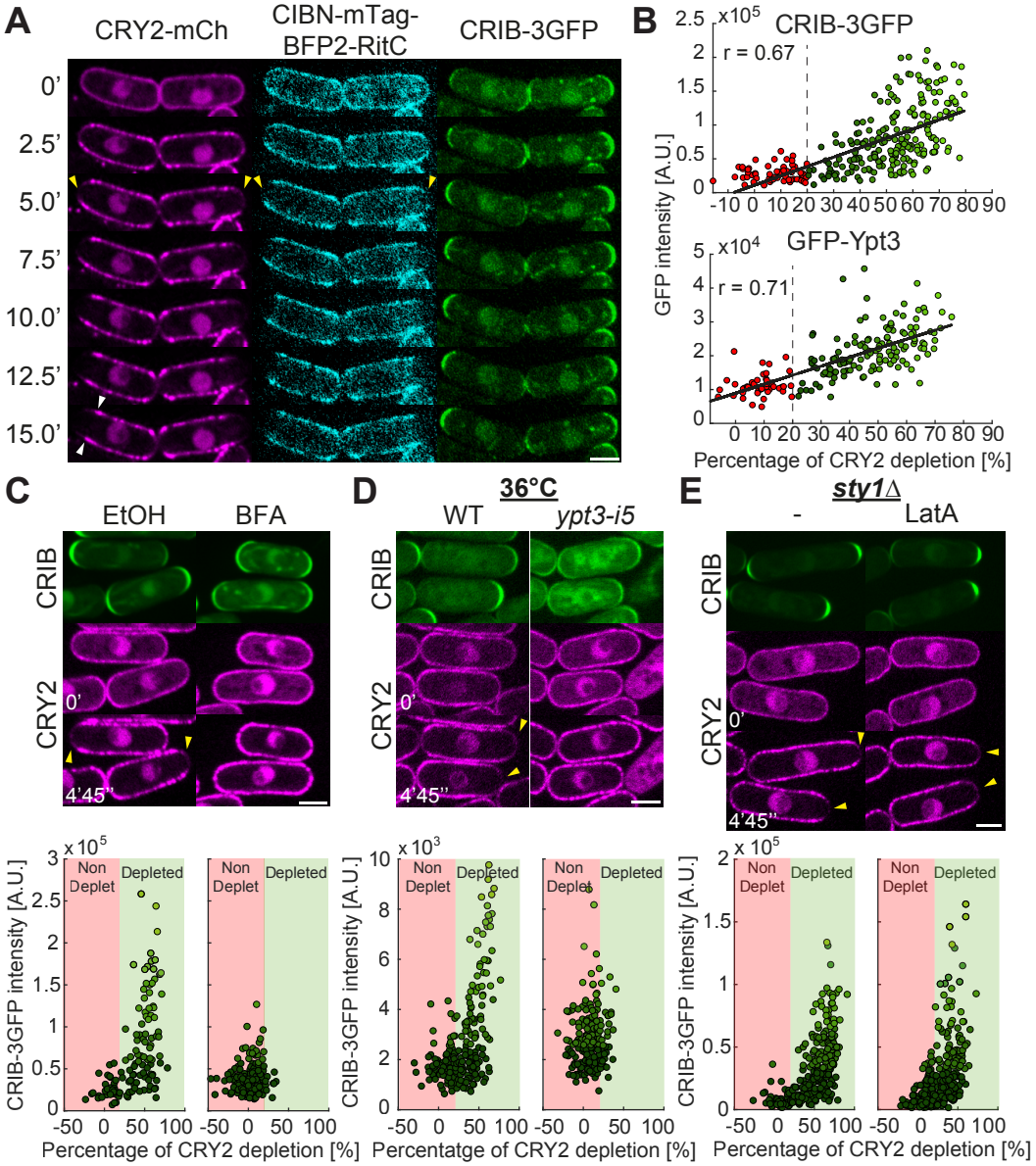

Figure 1. Depletion of membrane-associated CRY2 around sites of secretion
A. Time-lapse of CRY2-mCherry, CIBN-mTag-BFP2-RitC and CRIB-3GFP cells grown in the dark. Time 0 is the first timepoint after illumination. Yellow arrowheads indicate depletion zones. White arrowheads point to lateral peaks. **B.** Correlation plot of CRY2 depletion after 5 min and pole GFP intensity of CRIB-3GFP and GFP-Ypt3. Depletion cut-off is indicated by red to green colour change. **C-E.** Cells as in (A) treated with 300µM brefeldin A (BFA) or solvent (EtOH) (C), carrying or not *ypt3-i5* grown at 36°C for 30 min (D) or carrying a *sty1* deletion (*sty1*Δ) treated or not with 50µM Latrunculin A (LatA) (E). The GFP channel is a 5-min temporal sum projection. mCherry shows individual time points. Bottom graphs are as in (B). Data points are coloured with different shades of green according to GFP fluorescence. Scale bars are 3µm in all figures.

Figure 2

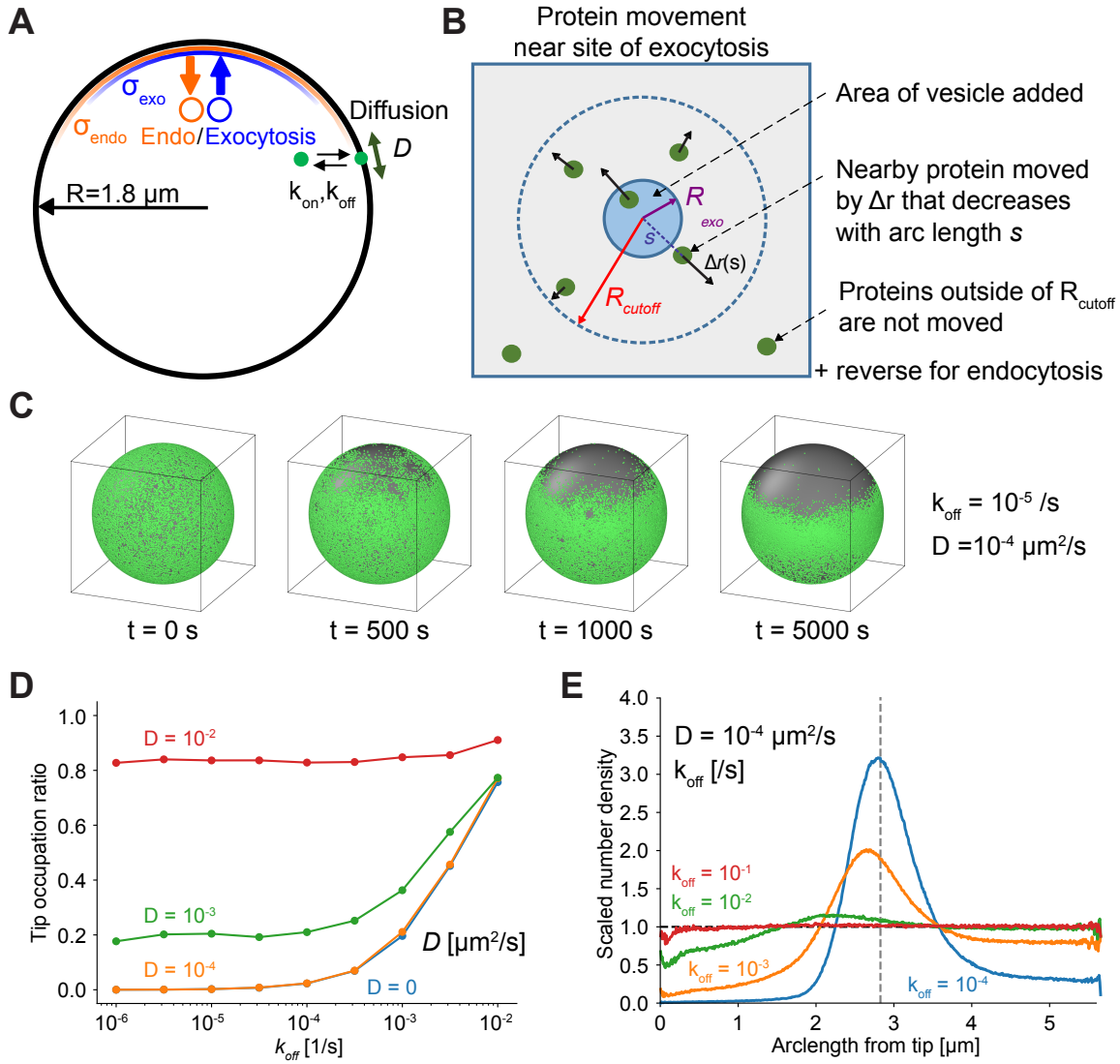

Figure 2. Simulations of membrane-flow-induced concentration gradients
A. Particles representing proteins have diffusion coefficient D on a spherical cell and exchange with a uniform internal pool with rates k_{off}, k_{on}. Exocytosis (endocytosis) events occur with a distribution of width σ_{exo} (σ_{endo}) around a point representing cell tip. **B.** Particle displacement away/towards site of exocytosis/endocytosis. **C.** Depletion of particles starting from uniform distribution occurs for $\sigma_{exo} < \sigma_{endo}$, under static conditions (exocytosis rate = measured endocytosis rate). **D.** Tip occupation ratio vs k_{off} and D, same conditions as (C). **E.** Scaled number density vs arclength shows depletion and lateral peak near sphere equator at low k_{off} values.

Figure 3

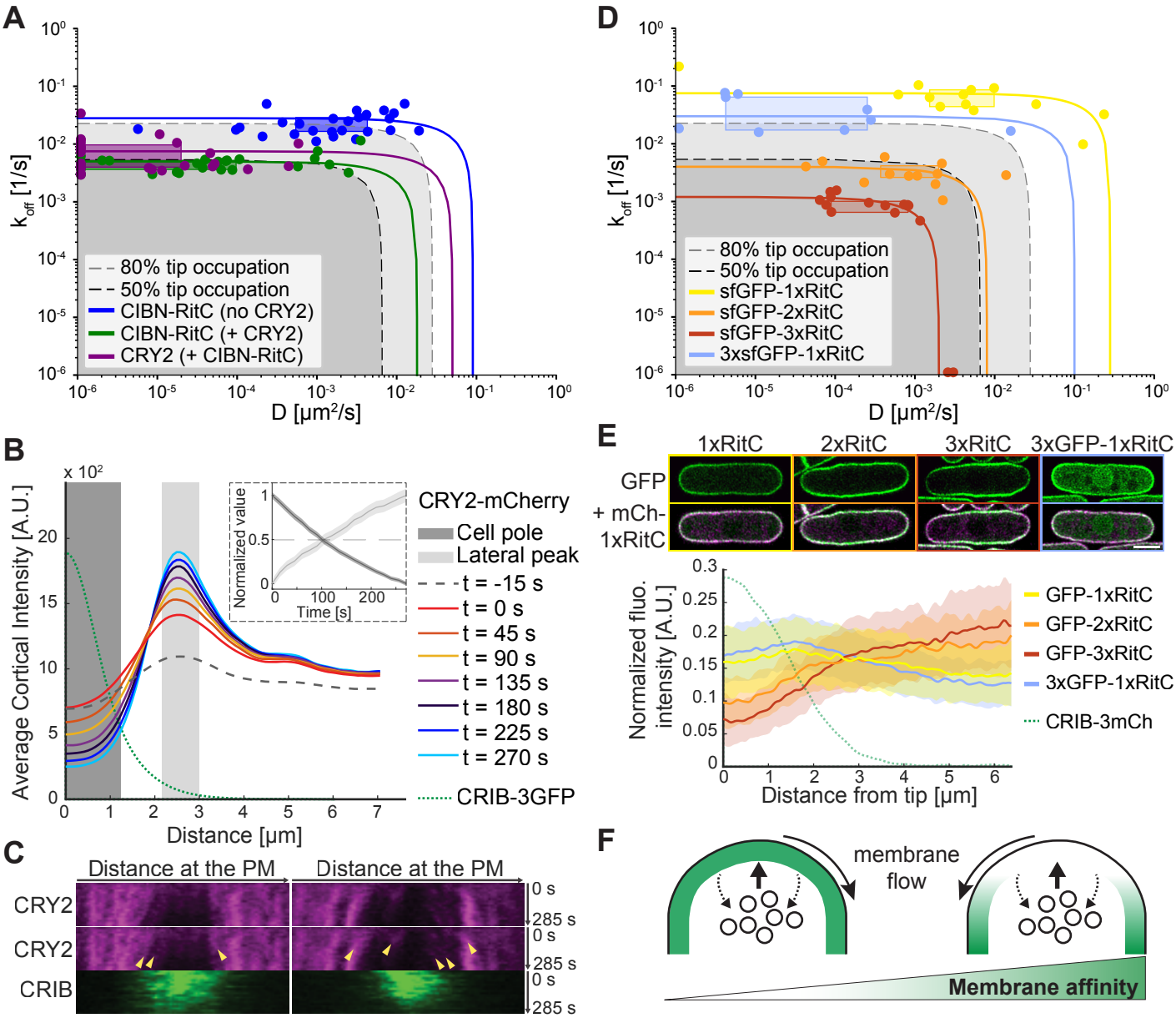

Figure 3. Experimental validation of membrane flows and affinity-dependent protein depletion. **A.** D and k_{off} of CIBN-RitC and CRY2 with or without CRY2 co-expression, derived from FRAP measurements. Points are best D and k_{off} fits for individual cells. Boxes are data point lower and upper quartiles. Lines show D and k_{off} combinations resulting in same overall FRAP recovery (from ridge of averaged R^2 data fits, Fig S4). Curved corner region corresponds to comparable contributions of D and k_{off}; outer limits to recovery dominated by diffusion or exchange. Grey shaded regions have predicted tip occupation below indicated levels (from growth condition simulations). **B.** CRY2 cortical profiles in time-lapse imaging as in Fig 1A. Time 0 is the first post-illumination image. Please compare to Fig 2E. The green dashed line shows the average CRIB distribution. The inset shows the average fluorescence value over time in the shaded areas. **C.** Kymographs of the cell pole in cells as in Fig 1A. **D.** D and k_{off} of indicated RitC constructs derived from FRAP measurements. Formatting is as in (B). **E.** Localization of indicated sfGFP-tagged RitC constructs in cells co-expressing mCherry-RitC. The graph shows sfGFP-RitC constructs and CRIB signal distribution (from cells as in Fig S6). **F.** Scheme of secretion-induced membrane flow, leading to associated protein depletion according to membrane affinity.

Figure 4

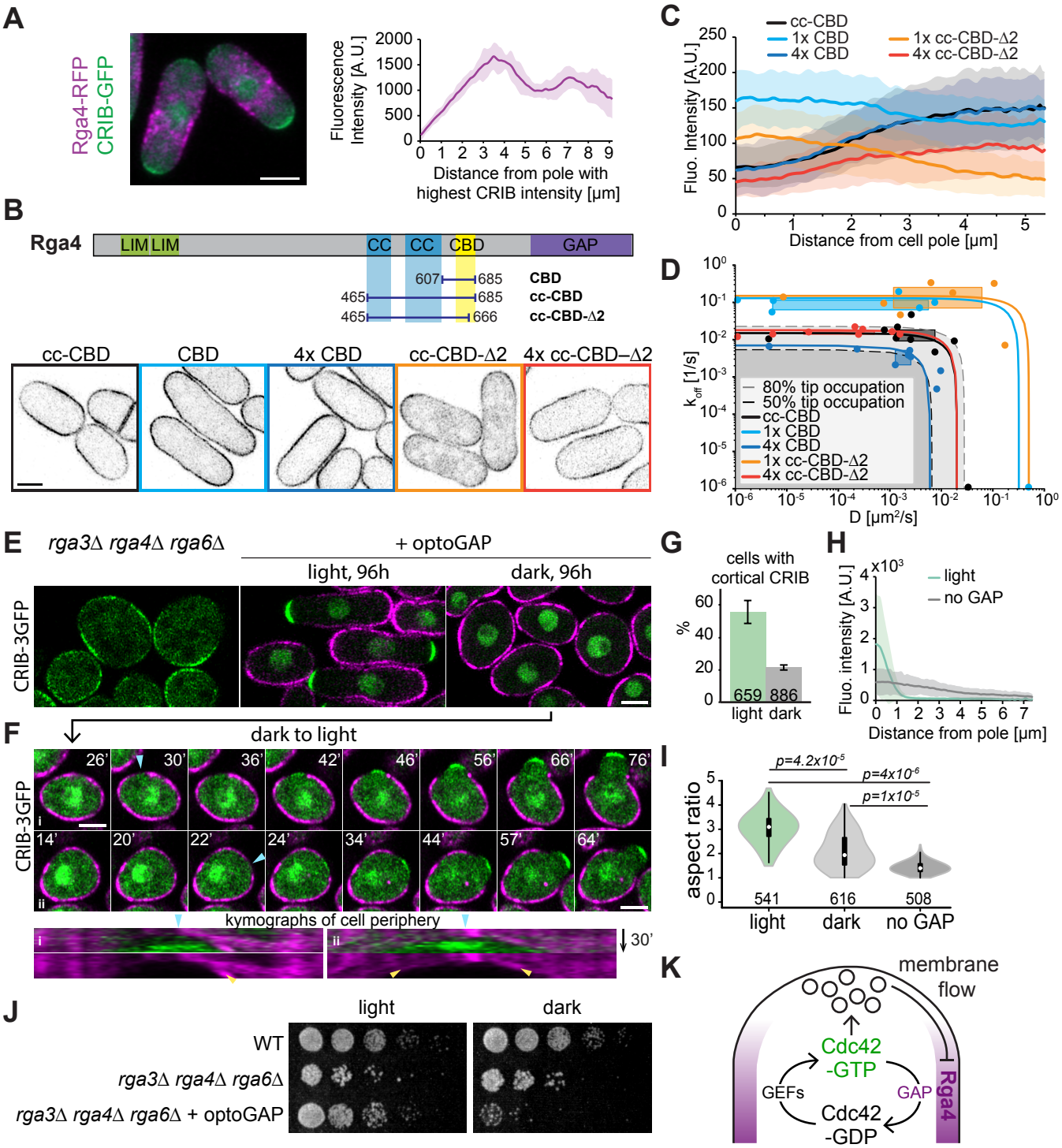

Figure 4. Membrane flow-induced Cdc42 GAP depletion forms a negative feedback restricting the secretion zone.

A. Maximum projection image of Rga4-RFP and CRIB-3GFP. The graph shows average and stdev of Rga4 distribution along cell length in 11 cells. **B.** Scheme and localization of the minimal cc-CBD Rga4 fragment, as well as single or 4x tandem CBD and cc-CBD-Δ2 constructs. **C.** Average cortical distribution of indicated constructs. Shaded areas show standard deviation. **D.** Diffusion and membrane detachment rates of Rga4 fragments as in (B) derived from FRAP measurements. Formatting as in Fig 3A. **E.** *rga3Δ rga4Δ rga6Δ CRIB-3GFP* cells expressing or not optoGAP continuously grown in the light or dark for 96h. **F.** Cells as in (E) grown in the dark and shifted to light at time 0. Arrowheads indicate optoGAP depletion. Kymographs show lateral movement of OptoGAP. **G.** Percentage of optoGAP-expressing cells as in (E) with local CRIB cortical signal. **H.** CRIB-GFP cortical profiles in light-grown optoGAP cells vs. cells not expressing optoGAP as in (E). **I.** Aspect ratio of cells as in (E). **J.** Serial dilution of indicated cells on rich medium. **K.** A double negative feedback regulates the size of the Cdc42-GTP zone. Cdc42-GTP promotes secretion, which induces membrane-associated flow of Rga4 GAP to cell sides where it restricts Cdc42 activation, thus constraining the Cdc42-GTP zone.